

# Lift Force Control of Flapping-Wing Microrobots Using Adaptive Feedforward Schemes

Néstor O. Pérez-Arancibia, *Member, IEEE*, John P. Whitney, and Robert J. Wood, *Member, IEEE*

**Abstract**—This paper introduces a methodology for designing real-time controllers capable of enforcing desired trajectories on microrobotic insects in vertical flight and hovering. The main idea considered in this work is that altitude control can be translated into a problem of lift force control. Through analyses and experiments, we describe the proposed control strategy, which is fundamentally adaptive with some elements of model-based control. In order to test and explain the method for controller synthesis and tuning, a static single-wing flapping mechanism is employed in the collection of experimental data. The fundamental issues relating to the stability, performance, and stability robustness of the resulting controlled system are studied using the notion of an input-output linear time-invariant (LTI) equivalent system, which is a method for finding an internal model principle (IMP) based representation of the considered adaptive laws, using basic properties of the  $z$ -transform. Empirical results validate the suitability of the approach chosen for designing controllers and for analyzing their fundamental properties.

**Index Terms**—Adaptive control, bio-inspired machines, flapping-wing flight, microrobots.

## I. INTRODUCTION

IN [1], the feasibility of flying robotic insects was empirically demonstrated. There, the lift-off of a 60-mg mechanical fly shows that bio-inspired flapping-wing robots can generate lift forces sufficiently large to overcome gravity. However, to date, detailed control strategies addressing altitude control have not been reported. Here, we propose a control scheme and a methodology for synthesizing controllers for the tracking of specified trajectories along the vertical axis. Evidence for the suitability of the considered scheme is provided through experimental results, obtained using the static single-wing flapping mechanism in [2].

The fundamental idea introduced in this work is that enough information about the subsystems composing the robotic insect can be gathered *a priori*, using well-known identification methods, such that, during flight, only an altitude sensor is required for controlling the microrobot. The two main subsystems relevant from a control perspective are the bimorph piezoelectric

driving actuator, used to transduce electrical into mechanical power, and the mapping, assumed static, from the actuator displacement to the average lift force generated by the passive rotation of the wing, as described in [2]. The system as a whole can be thought of as a *single-input-single-output* (SISO) dynamic mapping, where the input is the exciting voltage to the robot's driving actuator and the output is the resulting mechanical deformation of it. Since the actuator is mounted in the mechanical fly, this representation implicitly includes the dynamical interaction of the robot's rigid airframe with all the moving parts in the microrobot, which include the actuator, the transmission mechanism, the wing-hinge and the wing that dynamically interacts with the air. It is worth noting that the dynamics of this system are significantly different than the ones of isolated actuators [3]. Also, note that the static displacement-to-average-lift-force mapping is an abstract artifact used for design, but in reality this is a complex system composed of the mechanical transmission, the wing-hinge, and the wing interacting with the air to produce lift.

Inspired by nature [4], [5], but also for practical reasons, roboticists have commonly designed flapping-wing mechanisms to be excited by sinusoidal signals, mostly in open-loop configurations (see [1] and references therein). Here, we demonstrate the design and implementation of model-based and model-free controllers, in feedback and feedforward configurations, for following sinusoidal reference signals. The main idea is that, under actuator constraints, frequency, amplitude, and phase can be chosen and varied in order to achieve specifications of lift and power. Considering this design choice, a natural control strategy is the implementation of algorithms specialized in dealing with the tracking and rejection of periodic signals. In this category, there are the *internal model principle* (IMP) [6] based algorithms such as those in [7]–[11] and other related articles, and also the *adaptive feedforward cancelation* (AFC) algorithms such as those in [12] and [13] and references therein.

As a first approach to the problem, we adopt a control strategy based on a modified version of the discrete-time AFC algorithm in [12]. Since the AFC algorithm is a disturbance rejection scheme, here, the reference signals to be followed are treated as disturbances to be rejected. As in [12] and [13], the frequencies of the relevant signals are known while the amplitudes and phases are assumed unknown. The idea of treating the amplitudes and phases of sinusoidal references as unknowns seems counterintuitive. The reason for this design choice is that the general proposed control strategy for tracking a specified average lift force signal, or a desired altitude signal, generates in real time a required amplitude for a fixed frequency.

Manuscript received December 7, 2010; revised May 12, 2011; accepted July 19, 2011. Date of publication September 15, 2011; date of current version September 12, 2012. Recommended by Technical Editor J. Xu. This work was supported by the Office of Naval Research under Grant N00014-08-1-0919.

The authors are with the School of Engineering and Applied Sciences, Harvard University, Cambridge, MA 02138 USA, and also with the Wyss Institute for Biologically Inspired Engineering, Harvard University, Boston, MA 02115 USA (e-mail: nperez@seas.harvard.edu; jwhitney@fas.harvard.edu; rjwood@eecs.harvard.edu).

Color versions of one or more of the figures in this paper are available online at <http://ieeexplore.ieee.org>.

Digital Object Identifier 10.1109/TMECH.2011.2163317

As it will be explained later in this paper, the approach followed in this work is reminiscent of what in the biology literature is referred to as amplitude modulation [5]. From an engineering perspective, the relevant idea introduced here is that the fixed frequency of a periodic reference signal is chosen through experiments that give us information about the mathematical relationship between the actuator output and the resulting average lift force. In this case, with the use of the modified AFC scheme, a look-up table is estimated. Thus, control strategies for hovering and vertical flight can be devised using the experimentally estimated look-up table, in combination with an upper level control law and a model-based AFC scheme. Alternatively, measured information of the microrobot's altitude can be used directly for control.

The rest of the paper is organized as follows. Section II explains the microrobotic flapping mechanism, the experimental setup, and motivates the use of such a system. Section III describes the system identification of the biomorph actuator connected to the airframe and to the transmission, which is one of the relevant subsystems for controller design. Section IV discusses the considered control strategies and presents a method for evaluating the closed-loop system's stability, performance, and stability robustness. Section V presents experimental evidence on the suitability of the proposed methods. Finally, conclusions are given in Section VI.

#### Notation:

- 1) As usual,  $\mathbb{R}$  and  $\mathbb{Z}^+$  denote the sets of real and nonnegative integer numbers, respectively.
- 2) The variable  $t$  is used to index discrete time, i.e.,  $t = \{kT_s\}_{k=0}^{\infty}$ , with  $k \in \mathbb{Z}^+$  and  $T_s \in \mathbb{R}$ . As usual,  $T_s$  is referred to as the sampling-and-hold time. Depending on the context, we might indistinctly write  $x(t)$  or  $x(k)$ .
- 3) The variable  $\tau$  is used to index continuous time. Thus, for a generic continuous-time variable  $x(\tau)$ ,  $x(t)$  is the sampled version of  $x(\tau)$ .
- 4)  $z^{-1}$  denotes the delay operator, i.e., for a signal  $x$ ,  $z^{-1}x(k) = x(k-1)$  and conversely  $zx(k) = x(k+1)$ . In Subsection IV-B, for convenience,  $z$  is also the complex variable associated to the  $z$ -transform.

## II. MOTIVATION AND DESCRIPTION OF THE EXPERIMENTAL SYSTEM

### A. Motivation

An important intermediate objective in our research is altitude control of a microrobotic fly such as the one in [1], depicted in Fig. 1. A fundamental difficulty in achieving this goal is that due to constraints of space and weight, no internal sensors are considered to be mounted in the current iteration of the micro-robot. Instead, our design relies on off-line system identification of the subsystems composing the robot, and also in some cases, on an external position sensor.

It can be shown that the control objective in the previous paragraph can be translated into one of lift force control, and finally as shown in Section IV, reduced to an actuator output control problem. A first thing to notice is that from Fig. 1, the dynamical equation governing the movement of the fly along

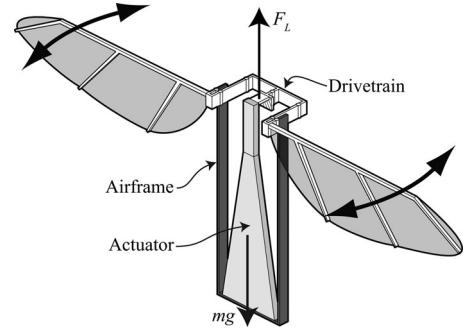


Fig. 1. Illustration of a typical Harvard Microrobotic Fly, similar to the one in [1]. This particular design is described in [14] (drawing courtesy of P. S. Sreetharan).

the vertical axis is simply

$$f_L - mg = m\ddot{x} \quad (1)$$

where  $m$  is the mass of the fly,  $g$  is gravitational acceleration and  $f_L$  is the instantaneous lift force generated by the flapping of the wings. In some cases, an additional dissipative body drag term  $\kappa_d \dot{x}$  could be added to the right side of (1), where  $\kappa_d$  is a constant to be identified experimentally.

As described in [2], the lift force  $f_L$  is a nonlinear function of the frequency and amplitude of the flapping angle. And, as also discussed in [2], for sinusoidal inputs,  $f_L$  forces typically oscillate around some nonzero mean force, crossing zero periodically. Therefore, ascent occurs when in average the lift force  $f_L$  is larger than  $mg$ . When using digital computers for measurement and control,  $f_L$  will be sampled at a fixed sampling rate  $T_s$ . Therefore, mathematically, the average force can be written as

$$\begin{aligned} F_L^{(N_L)}(t) &= F_L^{(N_L)}(kT_s) = F_L^{(N_L)}(k) \\ &= \frac{1}{N_L} \sum_{i=0}^{N_L-1} f_L(k-i) \end{aligned} \quad (2)$$

where,  $0 < N_L \in \mathbb{Z}^+$ . Often, the superscript  $(N_L)$  will be dropped and we will simply write  $F_L(t)$ , if  $N_L$  is obvious from the context.

Thus, the key element in our control strategy is the capability of forcing the average lift force signal in (2) to follow a specified reference. In order to develop a general methodology to be applied to any flapping-wing microrobot of the kind depicted in Fig. 1, here, we propose and study algorithms and techniques for identifying the plants of the relevant subsystems and tuning the necessary parameters involved. This is done using a modified version of the experimental setup in [2], which is discussed in the next subsection.

### B. Experimental Setup

We use the experimental setup in Fig. 2, which is a modified version of the one in [2]. This setup was constructed for the simultaneous measurement of lift forces generated by a flapping mechanism and the system identification of the biomorph actuator dynamics, when connected to the airframe and to the

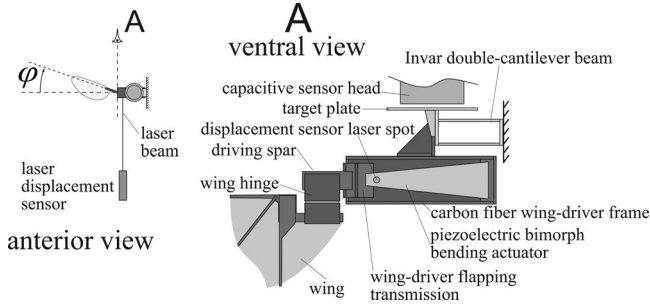


Fig. 2. Diagram of experimental setup for measuring lift forces and actuator displacements. The wing-driver is attached to an Invar double-cantilever beam, whose deflection is measured by a capacitive displacement sensor. This deflection is proportional to the lift force. The actuator displacement is measured using a CCD laser displacement sensor (LK-2001 fabricated by Keyence). For details on the force sensor see [15].

transmission mechanism. In Fig. 2, it can be observed that the wing driver mechanism is mounted on the end of a double-cantilever beam, whose deflection is measured with a *capacitive displacement sensor* (CDS). From solid mechanics principles, for small beam deflections, there is a linear relationship between deflection and lift force.

The wing is flapped using a piezoelectric bimorph actuator, similar to the one described in [16], mounted to a carbon fiber frame. The linear displacement of the drive actuator is mapped to an angular flapping motion employing a transmission mechanism of the type described in [1]. The resulting flapping angle is labeled by  $\varphi$  in Fig. 2. Notice that as explained in [2], flapping induces the flexure of the wing-hinge, generating the passive rotation that in turn produces lift. In order to minimize the effective mass of the beam-driver system, the actuator's geometry is optimized for energy density, resulting in a lightweight actuator and maximal sensor bandwidth. Further details on the design, fabrication, and calibration of the CDS-based force sensor are given in [2] and [15].

The other variable measured is the deformation of the actuator tip. As shown in Fig. 2, this is done using a noncontact CCD<sup>1</sup> laser displacement sensor (LK-2001 fabricated by Keyence), which is located at a close distance from the distal portion of the actuator. In Fig. 2, the sensor laser reflection on the actuator is depicted as a circular spot.

### III. SYSTEM IDENTIFICATION FOR CONTROLLER DESIGN

#### A. Identification of the System Dynamics

The flapping mechanism described in Section II can be seen, from the piezoelectric actuator perspective, as a system in which the input is the voltage signal to the actuator and the output is the displacement of the distal end of the actuator, measured using the CCD laser displacement sensor. In this approach, the output disturbance  $v(t)$  represents the aggregated effects of all the disturbances affecting the system, including the unmodeled aerodynamic forces produced by the wing flapping. With this idea in mind, as depicted in Fig. 3, a discrete-time representation

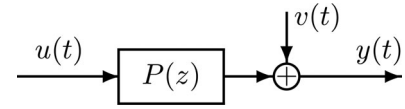


Fig. 3. Idealized system dynamics.  $P(z)$ : Identified discrete-time open-loop plant;  $u(t)$ : Input voltage signal to the actuator;  $y(t)$ : Output actuator displacement;  $v(t)$ : Output disturbance, representing the aggregated effects of all the disturbances affecting the system, including the unmodeled nonlinear aerodynamic forces produced by wing flapping.

of the system can be found using *linear time-invariant* (LTI) system identification methods. It is important to emphasize that the dynamics of this system are significantly different to the ones of isolated actuators [3].

Thus, using the algorithm in [17], according to the implementation described in [18] and [19], the system modeled in Fig. 3 is identified, using 200 000 samples generated using a white-noise signal input  $u(t)$ , at a sampling-and-hold rate of 10 KHz. Note that due to variability in the microfabrication process, the models shown in this article are used to illustrate the proposed identification and control strategies, but they do not necessarily represent the typical dynamics of flapping systems.

The identified dynamics of  $P(z)$ , labeled as  $\hat{P}(z)$ , are shown in Fig. 4. There, the original 48th-order model is shown along with reduced models with orders 12 and 4, respectively. Notice that the identified systems have been normalized so that the respective DC gain is 0 dB. The natural frequency of  $\hat{P}(z)$  is 118.36 Hz. As usual, in order to reduce the system, a state-space realization of the identified 48th-order model is balanced [20], and then, a certain number of states, relatively less observable and controllable than the others, are discarded. For theoretical details on linear system theory, system identification and control see [20]–[27] and [28]; for comments on an experimental implementation see [18] and [19]. The resulting 4th-order reduced identified LTI system dynamics are given by

$$x_P(k+1) = A_P x_P(k) + B_P u(k) \quad (3)$$

$$y(k) = C_P x_P(k) + D_P u(k) \quad (4)$$

with the matrices  $\{A_P, B_P, C_P, D_P\}$  in the Appendix.

Notice that since the system identification is performed with the actuator mounted to the airframe and connected to the transmission mechanism, the frequency response in Fig. 4 does not capture the dynamics of the actuator, but the coupled dynamics of the actuator-transmission-wing-airframe system.

### IV. CONTROL STRATEGIES

#### A. Actuator Displacement Control

In some studies of biological flapping-flight [5], [29], [30], the mean total force,  $\Phi_T$ , generated by a wing (or a symmetrical wing pair) throughout the stroke is estimated as

$$\Phi_T = \int_0^{\Xi} \rho \overline{C_\Phi} \overline{v_r^2}(\xi) c(\xi) d\xi \quad (5)$$

which is a standard quasi-steady blade-element formulation of flight force (see [2] and references therein), where  $\rho$  is the density of the air ( $1.2 \text{ Kg} \cdot \text{m}^{-3}$ , [5]),  $\overline{C_\Phi}$  is the mean force

<sup>1</sup>Charge-coupled device.

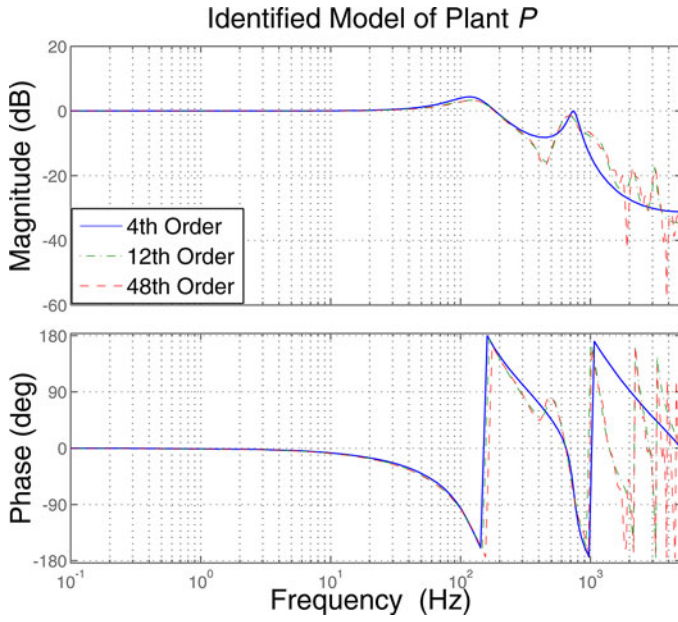


Fig. 4. Bode diagram of identified model  $\hat{P}(z)$  of the plant  $P(z)$ . A 48th-order model is shown in red, reduced 12th and 4th order models are shown in green and blue, respectively.

coefficient of the wing throughout the stroke,  $\overline{\nu_r^2}(\xi)$  is the mean square relative velocity of each wing section,  $c(\xi)$  is the chord length of the wing at a distance  $\xi$  from the base, and  $\Xi$  is the total wing length. Note that assuming a horizontal stroke plane, for a sinusoidal stroke  $\varphi(\tau) = \varphi_0 \sin(2\pi f_r \tau)$ , the relative velocity of the wing section can be estimated as

$$\nu_r(\tau, \xi) = \xi \dot{\varphi}(\tau) = 2\pi f_r \xi \varphi_0 \cos(2\pi f_r \tau) \quad (6)$$

which implies that the mean square relative velocity of each wing section can be roughly estimated as

$$\overline{\nu_r^2}(\xi) = 4\pi^2 f_r^2 \xi^2 \varphi_0^2 \frac{1}{T_r} \int_0^{T_r} \cos^2(2\pi f_r \tau) d\tau \quad (7)$$

with  $T_r = f_r^{-1}$ . Thus, it immediately follows that

$$\overline{\nu_r^2}(\xi) = 2\pi^2 \xi^2 \varphi_0^2 f_r^2 \quad (8)$$

which implies that regardless of the size and shape of the wing (or symmetrical wing pair), the estimated mean total flight force directly depends on  $f_r^2$  and  $\varphi_0^2$ . This indicates that in order for flying insects to accelerate against gravity or hover at a desired altitude, they can modulate the output average lift force by changing the stroke amplitude,  $\varphi_0$ , or by changing the stroke frequency  $f_r$ . The first phenomenon is referred to as *amplitude modulation* and the second as *frequency modulation*.

In the problem considered here, the model in (5) is not practical for designing a general control strategy, because it explicitly depends on the morphology of the particular system to be controlled. However, we can use (8) as a general guideline from which we can inspire control strategies. As commented in Section II, for the robots considered here, the transmission that maps the actuator displacement  $y(t)$  to the stroke angle  $\varphi(t)$  can be approximated by a constant  $\kappa_T$ , i.e.,  $\varphi(t) = \kappa_T y(t)$ . Thus,

changing the amplitude and/or the frequency of  $y(t)$ ,  $\Phi_T$  can be modulated. Here, we propose a control strategy that can be used for amplitude modulation or frequency modulation. However, we mostly concentrate on amplitude modulation.

Note that in steady state, the average lift force  $F_L(t)$  can be thought of as an estimate of  $\Phi_T$ . As explained in Section II, in order for a robotic insect to follow a desired trajectory, a reference  $F_L^*(t)$  for  $F_L(t)$  must be followed. In the next subsection, we show that an empirical relationship between average lift force and amplitude of the actuator displacement, for a fixed frequency, can be found. A way of thinking about this relationship is as a lookup table, with which, for a given frequency, a desired average lift force is mapped into a desired amplitude to be followed by the actuator.

In order to implement a feedback control loop around  $P(z)$ , a measurement of the actuator displacement is required. However, in that case, a plant model is not strictly necessary for implementing the controller in real time. On the other hand, employing the identified plant  $\hat{P}(z)$  in Fig. 4, a model-based feedforward strategy can be pursued. A feedback control strategy is convenient in cases in which precision and accuracy are required. For example, when performing experiments in which relationships between actuator displacement and average lift force are estimated. A model-based feedforward strategy will be essential for the implementation of real-time controllers on systems in which the use of displacement sensors for measuring the actuator output is infeasible with the available technology.

For reasons already commented, in both feedback and model-based feedforward configurations, the desired outputs from the system  $P(z)$  have the form

$$y_d(k) = a(k) \sin\left(\frac{2\pi k}{N}\right) + b(k) \cos\left(\frac{2\pi k}{N}\right) \quad (9)$$

where  $N \in \mathbb{R}$  is the number of samples per cycle, and  $a(k)$  and  $b(k)$  are considered unknown functions of time. The frequency is considered known. It is somehow counterintuitive to think of a reference as a partially unknown signal. However, this approach is convenient because in the lift force control experiments to be discussed later, the actuator displacement reference is generated in real time according to the lookup table to be discussed in Subsection IV-C, and therefore, unknown *a priori*.

As discussed in the Introduction section, here we use a slightly modified version of the discrete-time AFC algorithm in [12], which is an Euler method-based approximation of the continuous-time AFC algorithm studied in [31] and [32]. The proposed control scheme is shown in Fig. 5. For purposes of analysis, let us for now assume that  $v(k) = 0, \forall k$ . Then, the main idea behind the algorithm is that if the signal

$$r(k) = -y_d(k) \quad (10)$$

is effectively rejected, it follows that the error

$$e_y(k) = y(k) + r(k) = [Pu](k) + r(k) \quad (11)$$

is minimized. Consequently, if the error  $e_y(k)$  in (11) is minimized, the system output  $y(k)$  closely follows the reference  $y_d(k)$ .

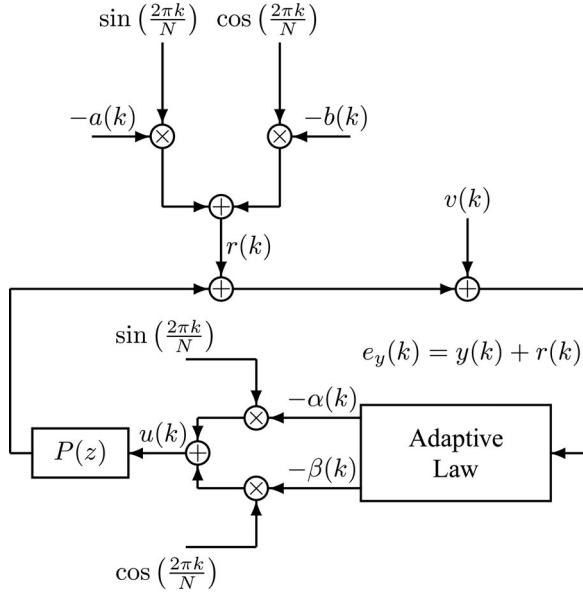


Fig. 5. Adaptive feedforward cancellation (AFC) scheme used for rejecting  $r(k)$  and tracking  $y_d(t)$ .

Ideally, for a stable minimum phase plant  $P$ , in order to cancel  $r(k)$ , the control signal should be  $u(k) = -[P^{-1}\hat{r}](k)$ , where  $\hat{r}(k)$  is an estimate of  $r(k)$ . However, most systems are non-minimum phase, in which instances, the best minimum phase approximation of  $P(z)$ ,  $\bar{P}(z)$ , should be used. In that case,  $\bar{P}^{-1}$  would produce an unwanted effect on the magnitude and phase of  $\hat{r}(k)$ . Fortunately, since the magnitude and phase of the periodic signal  $r(k)$  are being estimated adaptively, the system inverse can be ignored and the new control signal simply becomes

$$u(k) = -\left[\alpha(k) \sin\left(\frac{2\pi k}{N}\right) + \beta(k) \cos\left(\frac{2\pi k}{N}\right)\right] \quad (12)$$

with the adaptive law

$$\alpha(k) = \alpha(k-1) + \gamma e_y(k-1) \sin\left(\frac{2\pi k}{N} + \phi\right) \quad (13)$$

$$\beta(k) = \beta(k-1) + \gamma e_y(k-1) \cos\left(\frac{2\pi k}{N} + \phi\right) \quad (14)$$

where  $y(k)$  is the measured actuator displacement, and according to (11),  $e_y(k-1) = r(k-1) + y(k-1)$ . The symbol  $\gamma$  represents an adaptation gain, chosen with the use of computer simulations, employing a mathematical model of the system depicted in Fig. 5. The phase parameter  $\phi$  is also chosen with the use of computer simulations. Note that  $\gamma$  and  $\phi$  can be chosen analytically employing the method described in Subsection IV-B. Alternatively, both parameters can be tuned by the use of real-time experiments.

In this article, we introduce the notion that the reference signal  $r(k) = -y_d(k)$  in Fig. 5 can be seen as an output disturbance, and therefore, that the reference-following problem considered here is very similar to the disturbance rejection case in [13]. Note that since  $u(k)$  is filtered through  $P(z)$ ,  $\alpha(k)$  and  $\beta(k)$  are not estimates of  $a(k)$  and  $b(k)$ , respectively. Nonetheless, as

explained in [13], the ideas on stability and convergence for the input disturbance case, discussed in [12] and references therein, apply to this case.

Later in this subsection, we will show that a significant part of the frequency content of the disturbances affecting the microrobotic flapping system, for a sinusoidal input, modeled as the output disturbance  $v(t)$ , is the result of harmonics of the fundamental frequency  $f_r$ , where  $f_r$  is the frequency of the periodic signal  $r(t) = r(kT_s) = r(k)$  in Fig. 5. This nonlinear effect can be modeled by connecting a linear model and a polynomial mapping, in a so-called Volterra configuration, but, a compelling physical explanation behind this phenomenon is still lacking and this issue remains a matter of further research. Interestingly, the appearance of harmonics in natural insects has been reported [4], which suggests that there might be a fluid mechanics explanation of the phenomenon.

Disturbance profiles of this kind are reminiscent of the repeatable runout described in the *hard disk drive* (HDD) literature (see [11]–[13] and references therein). Thus, it is possible that the reasons for the appearance of harmonic disturbances in this case are similar to ones in the HDD case. Though the causes of this phenomenon are relevant for understanding the physics of the particular system, a compelling explanation is not necessary for the implementation of a scheme capable of rejecting the appearing harmonic disturbances. Thus, let us assume that

$$\begin{aligned} d(k) &= r(k) + v(k) \\ &= \sum_{i=1}^n \left[ a_i(k) \sin\left(\frac{2\pi ik}{N}\right) + b_i(k) \cos\left(\frac{2\pi ik}{N}\right) \right] \end{aligned} \quad (15)$$

where  $i \in \mathbb{Z}^+$  is the index corresponding to the harmonic  $i - 1$ , for  $i \geq 2$ . Clearly,  $n$  is also a finite positive integer. The real  $N$  is the number of samples per cycle and the reference signal is relabeled as  $r(k) = a_1(k) \sin\left(\frac{2\pi k}{N}\right) + b_1(k) \cos\left(\frac{2\pi k}{N}\right)$ . Obviously, the other components of  $d(k)$  in (15) are assumed to be part of  $v(k)$ .

Everything argued in the previous paragraphs, for the case  $d(k) = r(k)$ , is fundamentally valid for the case in which  $d(k) = r(k) + v(k)$  with the form in (15). Thus, as in [13], a canceling control signal for the case in (15) is

$$u(k) = -\sum_{i=1}^n \left[ \alpha_i(k) \sin\left(\frac{2\pi ik}{N}\right) + \beta_i(k) \cos\left(\frac{2\pi ik}{N}\right) \right]. \quad (16)$$

The update equations for the estimated parameters become

$$\alpha_i(k) = \alpha_i(k-1) + \gamma_i e_y(k-1) \sin\left(\frac{2\pi ik}{N} + \phi_i\right) \quad (17)$$

$$\beta_i(k) = \beta_i(k-1) + \gamma_i e_y(k-1) \cos\left(\frac{2\pi ik}{N} + \phi_i\right) \quad (18)$$

where the  $\gamma_i$  are adaptation gains, chosen differently for each harmonic. A phase advance modification can be added to reduce the sensitivity and allow for more harmonics to be canceled as was done previously in [12] and [13], if necessary. Sometimes it is convenient to pick  $\phi_i = \angle P(e^{j\theta_i})$ , where  $\theta_i = 2\pi i \left(\frac{f_r}{f_s}\right)$ , with  $f_r$  and  $f_s$  being the frequency of  $r(t)$  and the sampling

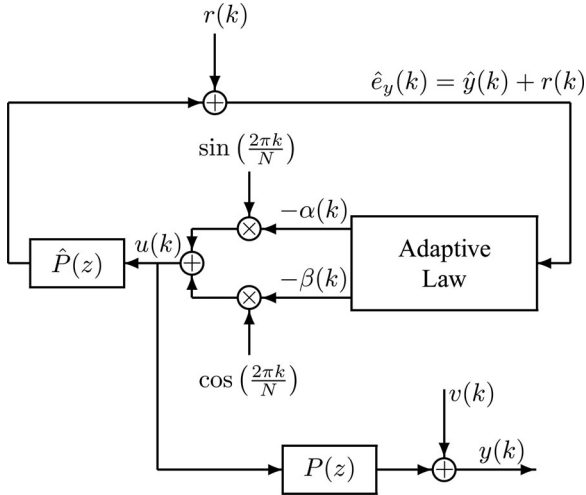


Fig. 6. Model-based AFC scheme for rejecting  $r(k)$  and tracking  $y_d(t)$ .

frequency of the system, respectively. As in the case where  $d(k) = r(k)$ , in this case,  $\alpha_i(k)$  and  $\beta_i(k)$  are not estimates of  $a_i(k)$  and  $b_i(k)$ .

Following the method in [12], and as done in [13], the adaptive feedforward disturbance rejection scheme in Fig. 5 can be transformed into an LTI equivalent representation. By treating the rejection scheme as an LTI system, the sensitivity function from  $d(k)$  to  $e_y(k)$  can be computed, allowing a performance evaluation of the whole system. Also using this LTI equivalent representation, the nominal stability and stability robustness of the system can be evaluated. These analyses are shown in Subsection IV-B. As it will be shown later in this article, the resulting LTI equivalent representations of the adaptive controllers also allows one to select an appropriate set of gains  $\{\gamma_i\}_{i=1}^n$ .

Due to limitations of space and weight, it is currently unreasonable to design a flying microrobot under the assumption that internal sensors can be mounted into the device. Therefore, here we explore the feasibility of implementing the scheme considered in Fig. 5 after replacing sensors by identified models, as shown in Fig. 6. There, the control signal  $u(k)$  is used as input to the system plant,  $P(z)$ , and also to an identified model of it,  $\hat{P}(z)$ . Instead of using the measured signal  $y(k)$  to update the gains  $\alpha(k)$  and  $\beta(k)$ , an estimate of  $y(k)$ ,  $\hat{y}(k)$ , is used.

In order to demonstrate the suitability of the proposed methods, we show four experimental cases in Figs. 7, 8, 9, and 10, respectively. The first case is shown for purposes of analysis and comparison, in which no control is applied to the system. Here, the system is excited in open loop by a sinusoidal signal  $u(t) = y_d(t) = A_r \sin(2\pi f_r t)$ , with normalized amplitude 1 and frequency  $f_r = 105$  Hz. The normalization is such that a constant input  $u(t) = 1$  generates an output equal to 1. Three things should be noticed in Fig. 7. The first is that the system can be approximated by the use of a linear model. This is clear from the fact that the *power spectral density* (PSD) estimate of the output  $y(t)$  shows that most of the signal power is concentrated at the fundamental frequency of the reference, 105 Hz. The second is that, as expected, the phase and magnitude of the output are changed with respect to the input. The third is that

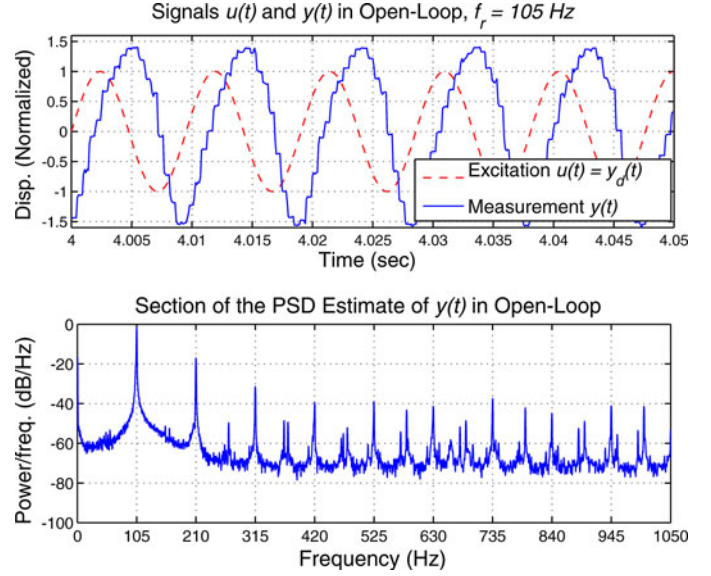


Fig. 7. **Case 1.** Upper Plot: Time series of  $u(t) = A_r \sin(2\pi f_r t)$  and  $y(t)$  in open loop, with  $A_r = 1$  and  $f_r = 105$  Hz. Bottom Plot: PSD estimate of the measured output  $y(t)$  in open loop.

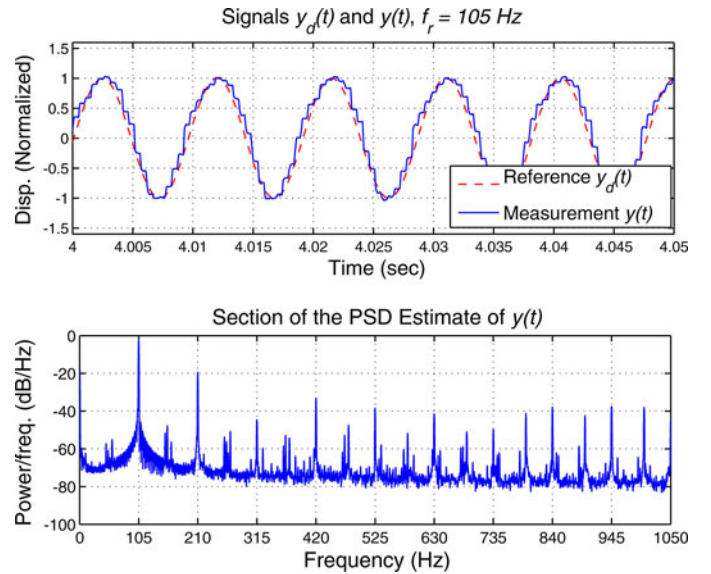


Fig. 8. **Case 2.** Upper Plot: Time series of  $y_d(t) = A_r \sin(2\pi f_r t)$  and  $y(t)$ , using the adaptive scheme in Fig. 5, with  $A_r = 1$  and  $f_r = 105$  Hz. Bottom Plot: PSD estimate of the measured output  $y(t)$ .

a pattern of harmonics appears in the output signal's PSD. As explained before, the physics of the underlying phenomenon is not completely understood. However, these harmonics can be treated as output disturbances affecting the system.

Cases 2 and 3 are shown in Figs. 8 and 9, respectively. In these cases,  $y_d(t) = A_r \sin(2\pi f_r t)$  and  $r(t) = -y_d(t)$ , with  $A_r = 1$  and  $f_r = 105$  Hz. Case 2 is the implementation of the adaptive scheme in Fig. 5, with the adaptive law in (12), (13), and (14). Clearly, the control strategy is capable of correcting for the phase shift and magnitude amplification, but as expected, the harmonics remain essentially the same of Case 1. Case 3 is the implementation of the adaptive scheme with the adaptive

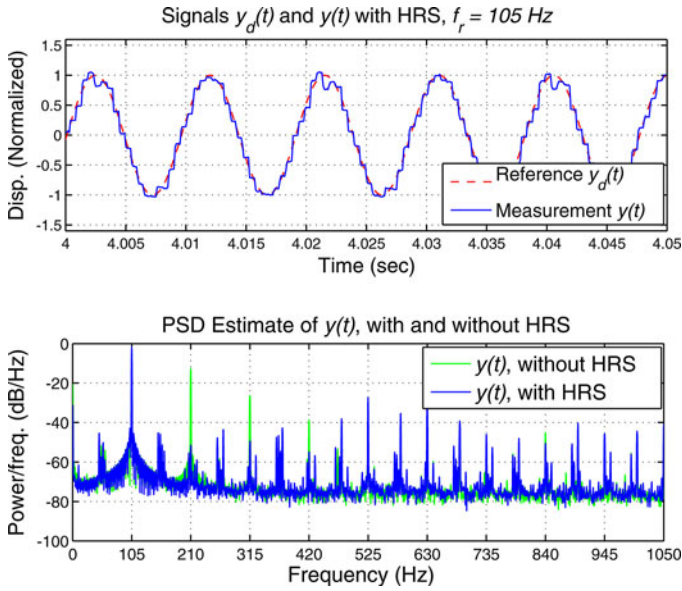


Fig. 9. **Case 3.** *Upper Plot:* Time series of  $y_d(t) = A_r \sin(2\pi f_r t)$  and  $y(t)$ , using the HRS, with  $A_r = 1$  and  $f_r = 105$  Hz. *Bottom Plot:* Comparison of the estimated PSDs of the measured outputs  $y(t)$ , with and without using the HRS.

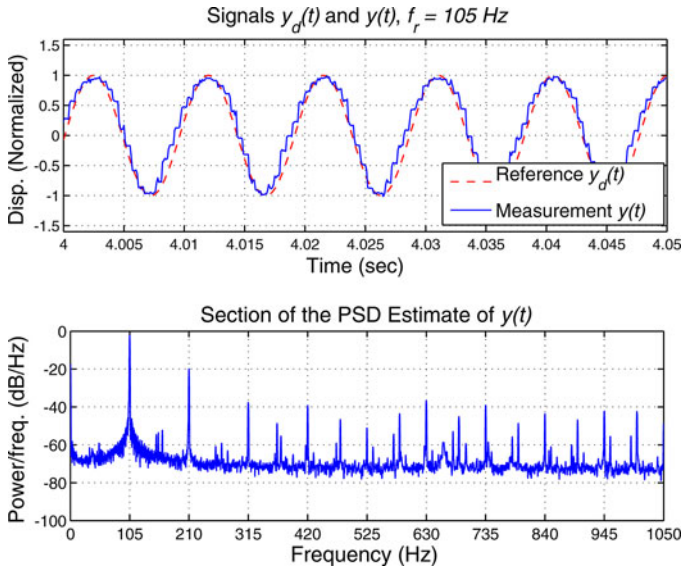


Fig. 10. **Case 4.** *Upper Plot:* Time series of  $y_d(t) = A_r \sin(2\pi f_r t)$  and  $y(t)$ , using the model-based adaptive scheme in Fig. 6, with  $A_r = 1$  and  $f_r = 105$  Hz. *Bottom Plot:* PSD estimate of the measured output  $y(t)$ .

law in (16), (17), and (18), which from this point onward is referred to as *harmonic rejection scheme* (HRS). Unequivocally, the control method is capable of correcting for the phase shift, the magnitude amplification, and also to reject the first three harmonics, which are the ones targeted in this experiment (i.e., it is assumed that  $n = 4$ ). These facts are evidenced by the bottom plot of Fig. 9, which compares the PSD estimates of the measured outputs  $y(t)$ , with and without using the HRS.

Finally, Case 4 is shown in Fig. 10. This is the implementation of the model-based AFC scheme in Fig. 6, with the same desired output  $y_d(t)$  of Case 2. In this case, the control signal  $u(k)$  is

TABLE I  
RMS VALUE OF THE CONTROL ERROR SIGNAL  $e_y(k)$ , FOR FOUR EXPERIMENTAL CASES

Case	1	2	3	4
RMS value	1.2107	0.1417	0.0867	0.1735

computed in real time employing the upper loop of Fig. 6, where  $\hat{e}_y(k) = \hat{y}(k) + r(k)$  is an estimate of  $e_y(k)$ . It is worth mentioning that the upper loop used to generate  $u(k)$  can be thought of as an economical way of storing an infinite amount of *a priori* known information about the system  $P(z)$ , which cannot be stored by a finite set of LTI feedforward controllers. Due to discrepancies between the model  $\hat{P}(z)$  and the physical system  $P(z)$ , the performance is degraded with respect to the ones obtained using the scheme in Fig. 5 and the HRS. However, this degradation is not significant in the context of this research. The control errors are summarized in Table I.

Note that for the kinds of problems addressed here, the adaptive schemes in Fig. 5 and Fig. 6 have several advantages. If a classical LTI strategy was to be pursued, the resulting controllers would be greatly limited by the constraints imposed by the *Bode integral theorem* [23], [24], and high performance would not be achievable over a wide frequency range. If a strategy based on repetitive control was to be pursued, variation of the reference frequency  $f_r$  in real time would be impossible.

### B. Equivalent LTI Model and Standard Analyses

In [32], using basic properties of the Laplace transform, it was shown that for the continuous-time version of the AFC algorithm, the operator mapping the input to the output of the adaptive controller is equivalent to an LTI system, for a fixed fundamental frequency. Here, for purposes of analysis, we find an LTI equivalent model of the operator from  $e_y(k)$  to  $u(k)$  in Fig. 5, using basic properties of the  $z$ -transform. Then, we use this result to study the stability of the system and for finding relevant sensitivity functions. Note that this analysis can be also used to find suitable adaptive gains for the scheme in Fig. 5. The method is similar to the one in [33], used to analyze a multiple error LMS algorithm. To begin with, notice that using the  $z$ -transform pair  $\mathcal{Z}\{\lambda^k x(k)\} = X(\lambda^{-1}z)$ , with  $\lambda$  a constant and  $\mathcal{Z}\{x(k)\} = X(z)$ , assuming zero initial conditions, it follows from (12) that

$$U(z) = \mathcal{Z}\{u(k)\} = -\frac{1}{2j} [A(e^{-j\omega}z) - A(e^{j\omega}z)] - \frac{1}{2} [B(e^{-j\omega}z) + B(e^{j\omega}z)] \quad (19)$$

where  $A(z) = \mathcal{Z}\{\alpha(k)\}$ ,  $B(z) = \mathcal{Z}\{\beta(k)\}$ , and  $\omega = \frac{2\pi}{N}$ . Similarly, from (13) and (14), assuming zero initial conditions, it follows that

$$A(z) = \frac{\gamma}{2j} \frac{z}{z-1} [e^{j\phi} \Delta(e^{-j\omega}z) - e^{-j\phi} \Delta(e^{j\omega}z)] \quad (20)$$

$$B(z) = \frac{\gamma}{2} \frac{z}{z-1} [e^{j\phi} \Delta(e^{-j\omega}z) + e^{-j\phi} \Delta(e^{j\omega}z)] \quad (21)$$

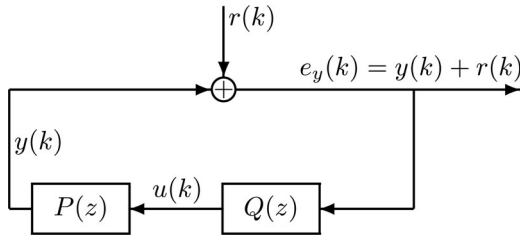


Fig. 11. Equivalent IMP-based LTI model of the AFC scheme in Fig. 5, assuming  $v(k) = 0, \forall k$ .

where,  $\Delta(z) = \mathcal{Z}\{\delta(k)\}$ , with  $\delta(k) = e_y(k-1)$ . Thus, from (19), (20), and (21) we obtain

$$U(z) = Q(z)E(z) = -\gamma \frac{z \cos \phi - \cos(\omega + \phi)}{z^2 - 2z \cos \omega + 1} E(z) \quad (22)$$

where,  $E(z) = \mathcal{Z}\{e_y(k)\}$ . Notice that here the symbol  $\delta(k)$  is used for convenience and this does not denote the Kronecker pulse signal.

Similar to the continuous-time case equivalence in [32], the LTI equivalence in (22) is remarkable, because the system given by (12), (13), and (14) is time-varying. More precisely, (22) states that the operator from  $e_y$  to  $u$  is equivalent to an LTI operator, although it is described by a set of linear time-varying difference equations. Notice that the filter  $Q(z)$  can be thought of as an IMP-based LTI controller in Fig. 5.

Thus, from an input-output mapping viewpoint, the adaptive control scheme in Fig. 5 is equivalent to the closed-loop LTI system in Fig. 11. In this way, the standard classical analyses, relating to the stability, performance and robustness of the system, can be carried out. In order to illustrate the point, here we consider the Cases 2 and 3 in the Subsection IV-A. In Case 2, the relevant parameters are  $\gamma = -0.001$ ,  $\phi = 0.4$  rad, and  $N = 95.2380$ . The mapping of main interest is the *error sensitivity function* (ESF), here defined as

$$S_e(z) = \frac{1}{1 - P(z)Q(z)} \quad (23)$$

where  $E(z) = S_e(z)R(z)$  and  $R(z) = \mathcal{Z}\{r(k)\}$ . Clearly,  $S_e(z)$  allows us to predict the performance of the system and also to test its stability. Note that  $S_e$  depends explicitly on the adaptive gain  $\gamma$ . In this context, a practical method for evaluating the performance of the system is to look at the depth of the ESF spectral notches. The idea is that for a specified frequency  $f_r$ , in order to minimize<sup>2</sup> the magnitude of  $e_y(k)$ , the gain between  $r(k)$  and  $e_y(k)$  should be as small as possible. An estimate of  $S_e(z)$ , computed as  $\hat{S}_e(z) = [1 - \hat{P}(z)Q(z)]^{-1}$ , is shown in Fig. 12, along with the frequency response of  $Q(z)$ . Notice that the filter  $Q(z)$  can be interpreted as a disturbance model of the reference signal  $r(k)$ , i.e., the spike in its Bode plot is approximately at 105 Hz (the spike is almost but not exactly at 105 Hz, because  $N = \frac{f_s}{f_r} = 95.2380$ ), which is expected from the internal model principle. Clearly, the spike in  $Q(z)$  becomes a notch in  $S_e(z)$ .

<sup>2</sup>Since no index has been defined, the word minimize is used in a colloquial sense.

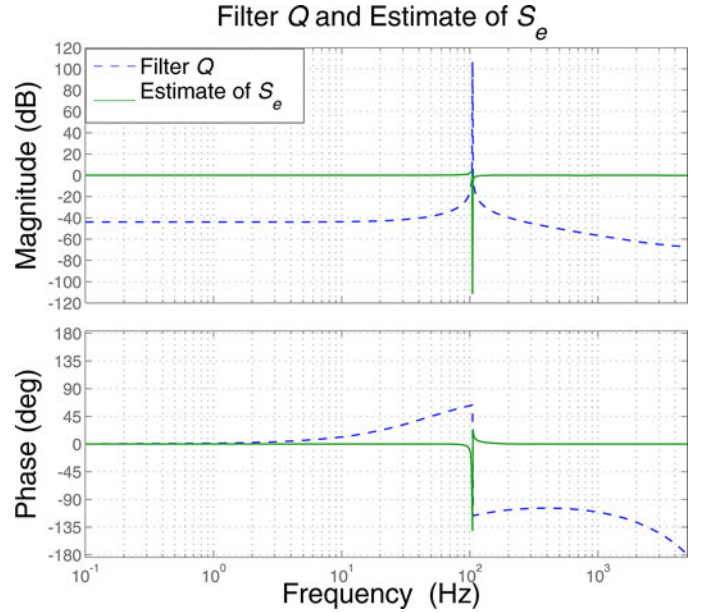


Fig. 12. Filter  $Q(z)$  and estimate  $\hat{S}_e(z) = [1 - \hat{P}(z)Q(z)]^{-1}$  of the error sensitivity function  $S_e(z)$ , using the LTI equivalent representation associated with Case 2.

The other mapping of interest is the loop-gain function defined as

$$L(z) = -P(z)Q(z) \quad (24)$$

which can be used to study the stability robustness of the system, using the classical indices gain and phase margins. Notice that since  $Q(z)$  depends on two chosen parameters,  $\gamma$  and  $\phi$ , its stability and robustness depend on these two parameters as well. In Case 2, as shown in Fig. 13, the system is robustly stable. This is in clear contrast with Case 3, in which the system is designed to follow reference  $y_d(k)$  and to cancel the first three harmonics, simultaneously.

In order to analyze the performance and stability robustness of the scheme employed in Case 3, first we repeat the analysis in the previous paragraphs, but considering  $d(k) = r(k) + v(k)$  with the form of (15). Therefore, assuming the adaptive law in (16), (17), and (18), the LTI equivalent mapping from  $e_y(k)$  to  $u(k)$  becomes

$$U(z) = Q(z)E(z) = \left[ -\sum_{i=1}^n \gamma_i \frac{z \cos \phi_i - \cos(\omega_i + \phi_i)}{z^2 - 2z \cos \omega_i + 1} \right] E(z) \quad (25)$$

where  $\omega_i = \frac{2\pi i}{N}$ ,  $\gamma_i$  and  $\phi_i$  are tuning parameters.

In the experiments of Case 3, the parameters are  $\gamma_1 = 0.001$ ,  $\gamma_2 = 0.001$ ,  $\gamma_3 = 0.0005$ ,  $\gamma_4 = 0.00001$ ,  $\phi_1 = 0.4$  rad,  $\phi_2 = 0$  rad,  $\phi_3 = -0.1$  rad, and  $\phi_4 = -0.8$  rad. Note that canceling additional harmonics requires an increasing tuning effort. Additionally, the stability robustness of the scheme can be decreased considerably with respect to Case 2. Fig. 14 shows the Bode plots of the resulting  $Q(z)$  and  $\hat{S}_e(z)$  associated with Case 3. There, once more the equivalence between the AFC scheme and

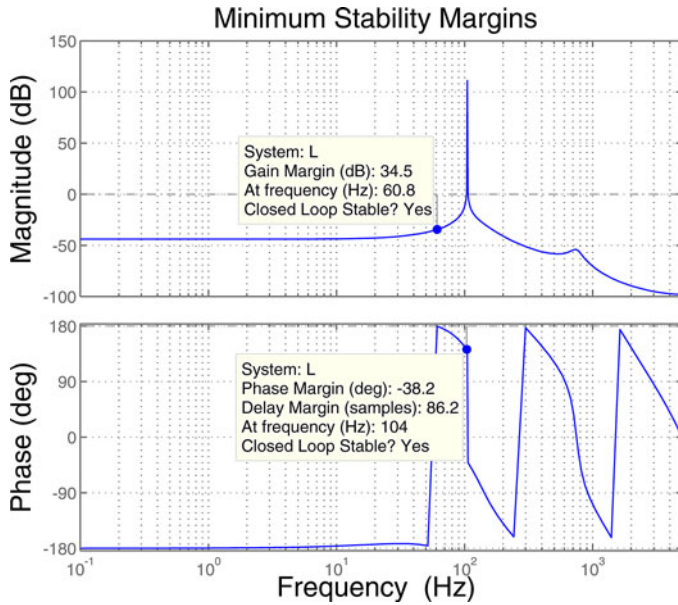


Fig. 13. Estimate  $\hat{L}(z) = -\hat{P}(z)Q(z)$  of the loop-gain function  $L(z) = -P(z)Q(z)$ , computed using the LTI equivalent representation associated with **Case 2**. The yellow tags indicate the classical minimum stability margins.

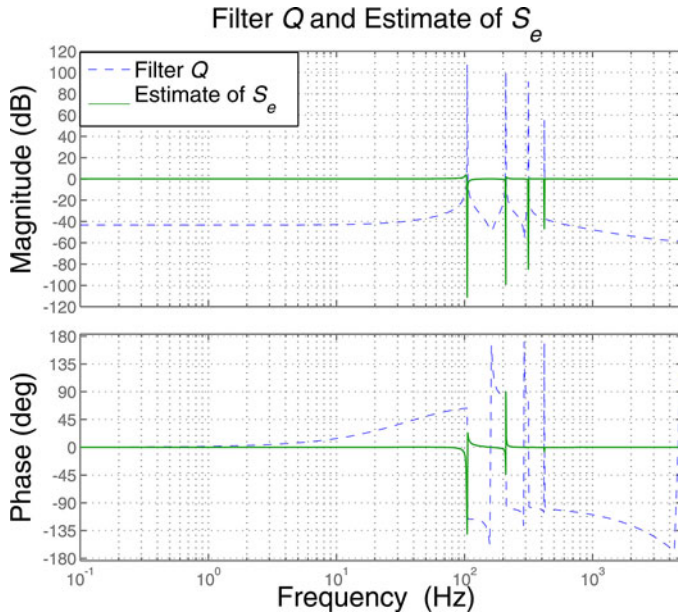


Fig. 14.. Filter  $Q(z)$  and estimate  $\hat{S}_e(z) = [1 - \hat{P}(z)Q(z)]^{-1}$  of the error sensitivity function  $S_e(z)$ , using the LTI equivalent representation associated with **Case 3**.

an LTI IMP-based controller can be observed. Notice that the shape of the ESF estimate  $\hat{S}_e(z)$  is consistent with the results shown in Subsection IV-A, in which the performance in Case 3 is significantly better than in Case 2. Unfortunately, there is a noticeable trade-off between performance and stability robustness, which can be observed in Fig. 15, due to a dramatic decrease of the phase margin value.

There is a subtle but important difference in the significance of the first notch in Fig. 14 relative to the other three notches. Notice

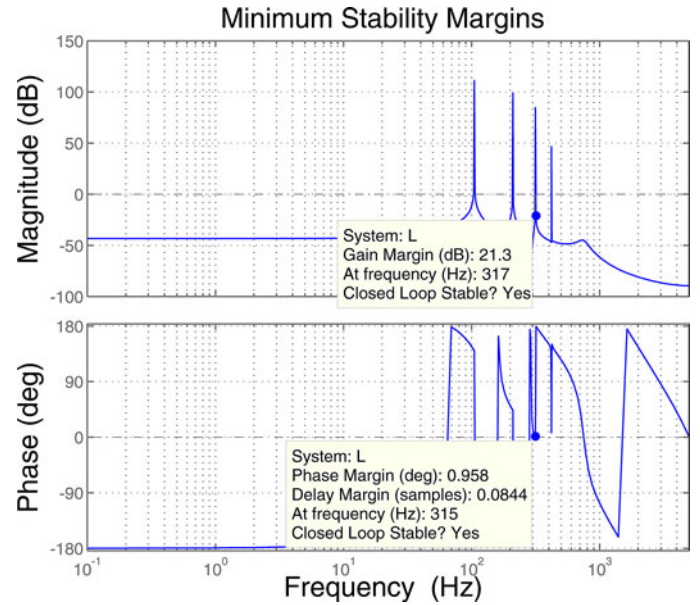


Fig. 15. Estimate  $\hat{L}(z) = -\hat{P}(z)Q(z)$  of the loop-gain function  $L(z) = -P(z)Q(z)$ , computed using the LTI equivalent representation associated with **Case 3**. The yellow tags indicate the classical minimum stability margins.

that from the problem formulation and from the analyses shown above, the magnitude of the first notch predicts how accurately the signal  $y(t)$  follows the reference  $y_d(t)$ , in the absence of disturbances and sensor noise. Differently, the magnitude of the other three notches predict how much the influence of the first three harmonics is attenuated in the signal  $y(t)$ . Also note that the LTI equivalent filters  $Q(z)$  in (22) and (25) directly depend on the tuning parameter  $\gamma$  and the set of tuning parameters  $\{\gamma_i\}_{i=1}^n$ , respectively. Therefore, the analysis presented in this subsection can be interpreted as an explicit description of a method for choosing the set of adaptive gains  $\{\gamma_i\}_{i=1}^n$ .

### C. Empirical Relationship Between Actuator Displacement and Lift Force

The considered control strategy relies on rejecting the signal  $r(k)$  by the use of the fully adaptive scheme in Fig. 5 or the model-based adaptive scheme in Fig. 6. In order to generate a signal  $r(t)$  with the appropriate phase and amplitude required for generating a desired average lift force profile, in this subsection we present an experimental method for finding a lookup table that maps the amplitude of the signal  $y(t)$  to the average lift force,  $F_L(t)$ , for fixed frequencies.

Arbitrarily, we pick five fixed values for the frequency  $f_r$ , 105, 120, 135, 150, and 180 Hz, and within these drive frequencies, the amplitude of  $y_d(t)$  is varied. Using the fully adaptive scheme in Fig. 5, we ensure that the actual output  $y(t)$  follows the chosen  $y_d(t)$ . Then, using the force sensor described in Section II, for a fixed frequency and a given amplitude, the average lift force is measured. For example, Fig. 16 shows the instantaneous and average forces when  $f_r = 105$  Hz, the amplitude of  $y_d(t)$  is equal to 1.2 and  $N_L = 1000$ . Repeating the experiment for different amplitudes, a mapping describing the amplitude-force

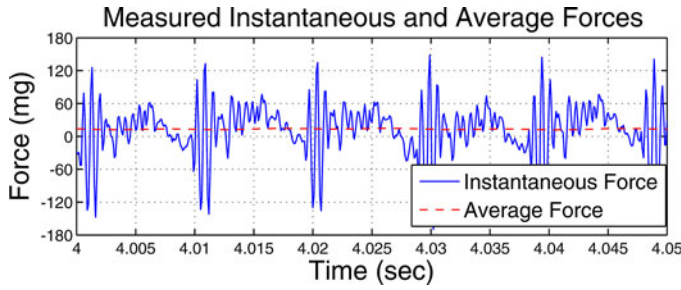


Fig. 16. Example showing instantaneous and average forces.

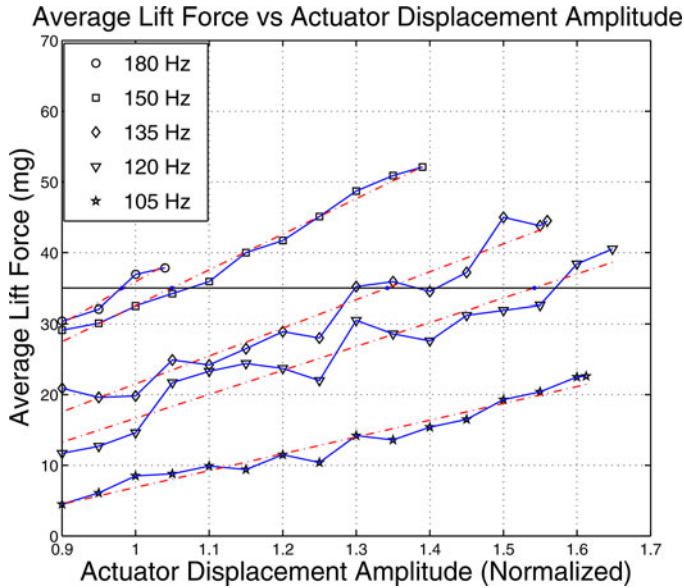


Fig. 17. Empirical relationship between the average lift force and the actuator displacement amplitude, with  $f_r$  taking the values 105, 120, 135, 150, and 180 Hz.

relationship can be found. Thus, for  $f_r = 105$  Hz, in Fig. 17 each symbol  $\star$  represents an experiment in which 200 000 data points were collected. There, it can be observed that the average lift force varies in a roughy linear manner on the signal  $y_d(t)$  amplitude. Then, using the least-squares method, a line is fitted to the data. This is shown as a dashed red line.

Besides its approximate linearity, another remarkable feature of the relationship between average lift force and the amplitude of  $y(t)$  is that the rightmost symbol  $\star$  marks the maximum actuator displacement amplitude achievable at the frequency  $f_r = 105$  Hz. The hard physical constraint is the amplitude of the control signal  $u(t)$  to the amplifier connecting the digital controller to the bimorph piezoelectric actuator. This signal cannot exceed 1 V, because it is amplified by a factor of 100 and biased by 100 V before connecting to the actuator, which by design does not tolerate voltages larger than 200 V. The maximum feasible amplitude of  $y(t)$  depends on the frequency  $f_r$ , and can be easily estimated by looking at the Bode plot of the identified plant  $\hat{P}(z)$  in Fig. 3.

The same experiment was repeated with  $f_r$  taking the values 120, 135, 150, and 180 Hz. The corresponding data points and fitted lines are shown in Fig. 17. Here, a couple of interesting

TABLE II  
RMS VALUE OF CONTROL SIGNAL  $u(k)$ , REQUIRED FOR GENERATING 35 mg OF LIFT FORCE

$f_r$	105 Hz	120 Hz	135 Hz	150 Hz	180 Hz
RMS value	Infeasible	0.9340	0.8606	0.7521	0.9408

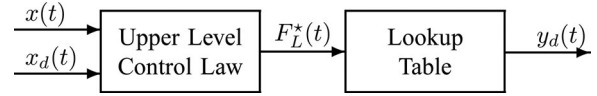


Fig. 18. Depiction of a generic upper level altitude control strategy.

things could be observed. The first is that around the natural frequency of the system  $P(z)$ , increasing the frequency  $f_r$ , increases the magnitude of the lift force. This is consistent with the notion that the lift force will increase with increasing wing velocities, at least within the range allowed for passive wing rotation to remain effective. As discussed in [2], and mentioned earlier in this article, the dynamics describing the relationship between flapping signals and lift forces are highly nonlinear. Therefore, the data shown here are for illustrating the proposed control scheme, and not for explaining a physical phenomenon, since these results are contingent to this particular experimental case. However, it is worth mentioning that the positive correlation between the value of the flapping frequency and the resulting average lift force in Fig. 17 is completely consistent with results previously reported [34].

With the previous comments in mind, a second thing to notice is that it is not necessarily the best control strategy to choose  $f_r$  equal to the natural frequency of  $P(z)$ . For example, among the options in Fig. 17, a good choice is  $f_r = 150$  Hz. To explain this statement consider the hypothetical case of a 70-mg fly, in which each wing should produce more than 35 mg of average force to generate a positive vertical motion. Clearly, more than 35 mg can be generated with amplitude 1 and  $f_r = 180$  Hz, amplitude 1.1 and  $f_r = 150$  Hz, amplitude 1.4 and  $f_r = 135$  Hz, and amplitude 1.6 and  $f_r = 120$  Hz. Notice that it is infeasible to generate a force larger than 35 mg with  $f_r = 105$  Hz. Therefore, a good choice is  $f_r = 150$  Hz, because it is not only possible to generate a lift force larger than 35 mg, but also because the maximum achievable force exceeds 50 mg, allowing a greater maneuverability. The RMS values of the required control signals for producing 35 mg are summarized in Table II. Notice that the required signal with smallest RMS value corresponds to the case  $f_r = 150$  Hz.

Note that in [2] a model relating the stroke angular trajectory ( $\varphi(t)$  in Fig. 2) to the passive rotation degree of freedom was found, assuming a fixed stroke plane. Relating actuator displacement to stroke angle is a function of the fixed transmission [3]. With the model in [2], lift forces can be estimated using a blade-element aerodynamic method. This model requires force and moment coefficients, which are typically derived experimentally, as their variation with wing shape, flexibility and flapping kinematics are not documented in the literature. Published coefficients for particular cases provide a good starting point. However, in the systems considered in this article, the

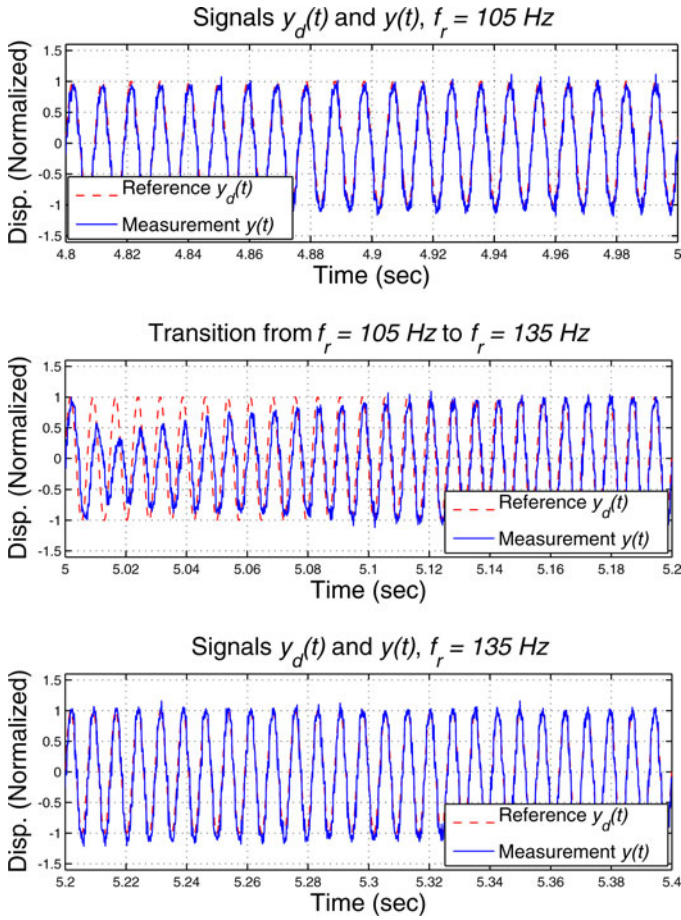


Fig. 19. Experimental example of a time-varying reference frequency  $f_r$ . This case shows in red the transition of  $y_d(t) = A_r \sin(2\pi f_r t)$  from  $f_r = 105$  Hz to  $f_r = 135$  Hz at  $Time = 5$  s. The resulting measurement  $y(t)$  is shown in blue.

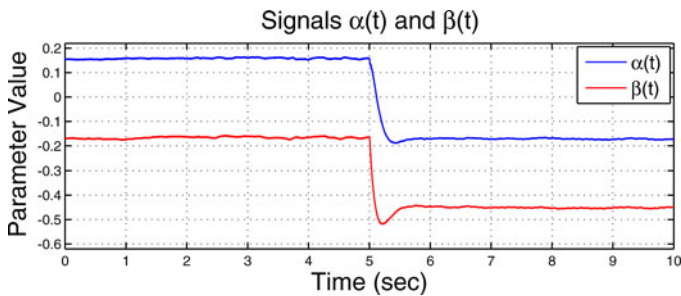


Fig. 20. Evolution of the adaptive parameters  $\alpha(t)$  and  $\beta(t)$ , corresponding to the experiment in Fig. 19. The first 5 s show the parameters in steady state, with  $f_r = 105$  Hz. At  $Time = 5$  s the value of the reference frequency  $f_r$  is changed from 105 Hz to 135 Hz. From  $Time = 5$  s to  $Time = 10$  s the plot shows the parameters' transition until they reach steady state, with  $f_r = 135$  Hz.

passive dynamics are also strongly influenced by the aerodynamic damping, which is not well studied or understood. For system modeling purposes, aerodynamic damping is empirically determined. Thus, in general, the modeling of aerodynamic systems simultaneously involves analysis and experimental estimation of parameters. In this article, we adopt an entirely experimental approach to obtain the models used for control, since

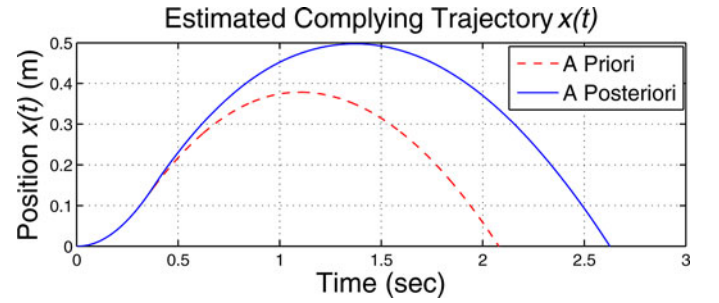


Fig. 21. *A priori* and *a posteriori* estimated complying trajectories.

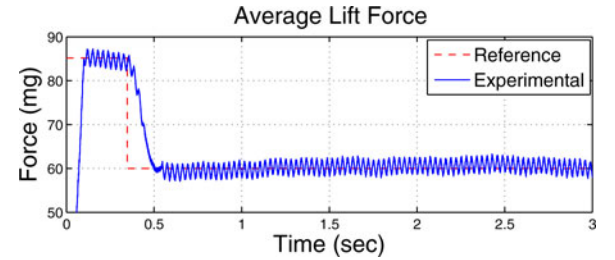


Fig. 22. Reference and experimentally obtained average lift force.

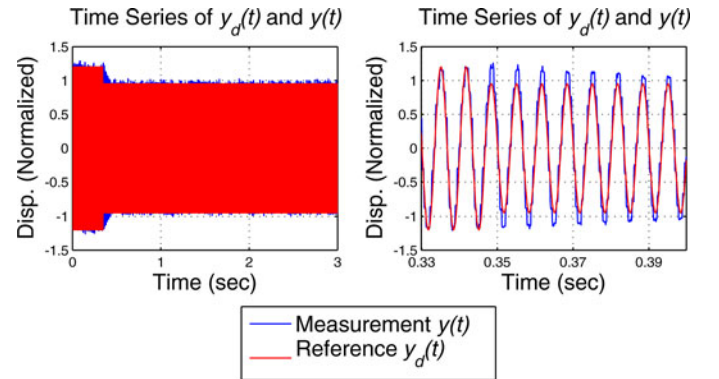


Fig. 23. Comparison of the time series of the experimental  $y_d(t)$  and  $y(t)$ , generating the average lift force in Fig. 22. *Left Plot*: Complete series. *Right Plot*: Transition from  $A_r = 1.2$  to  $A_r = 0.95$ .

the experimental setup provides reliable and accurate measurements for system identification. In the future, when passively rotating systems become better characterized, it will be reasonable to forgo system identification. Comparing predicted and identified plant dynamics will be important in future efforts, but is not the focus of this paper.

A controller which utilizes the empirical relationship between the actuator displacement and the generated average lift force is described in Fig. 18. Here,  $x(t)$  is the position of a fly as modeled in Subsection II-A, measured using an external sensor or camera and  $x_d(t)$  is the desired trajectory. Using  $x_d(t)$  or  $e_x(t) = x_d(t) - x(t)$  and an upper level control law, a desired average lift force  $F_L^*(t)$  can be generated. Then, using a lookup table, obtained empirically as was done in the cases shown in Fig. 17,  $F_L^*(t)$  is mapped to a desired reference  $y_d(t)$  to be used in the scheme in Fig. 6. Two experimental examples are described in the next section.

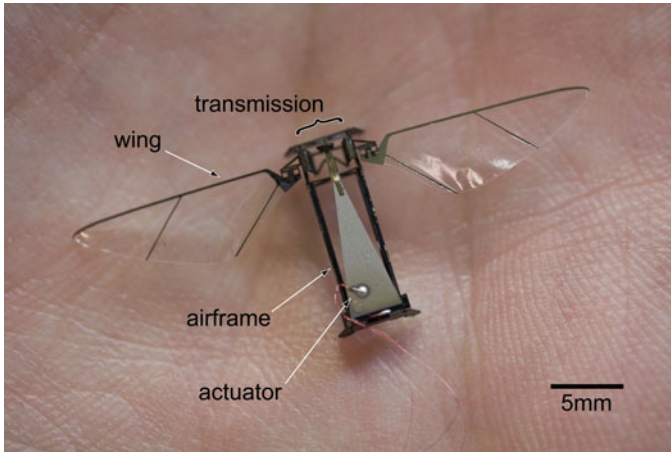


Fig. 24. Photograph of the flapping-wing flying microrobot used in the hovering experiments.

#### D. Time-Varying Reference Frequency

This subsection is a deviation from the main topic treated in this article. Here, we show the capability of the scheme in Fig. 5 of following a frequency varying reference signal  $y_d(t)$ . As explained previously, as a design choice, we employ amplitude modulation of the actuator motion in order to follow a desired average lift force  $F_L^*(t)$  or desired altitude  $x_d(t)$ . From Fig. 17, it is clear that in order to change the generated average lift force in real time, a feasible strategy is to fix the frequency of a desired output  $y_d(t) = A_r \sin(2\pi f_r t)$  and then choose, according to an upper-level control law (as depicted in Fig. 18) and the look-up table in Fig. 17, the required  $A_r$ . As shown before, all this is possible by either using the scheme in Fig. 5, the information in Fig. 17 and the measurement  $y(t)$ , or alternatively, by using the scheme in Fig. 6, the information in Fig. 17 and the model  $\hat{P}(z)$ .

An alternative to the previously described approach is the use of frequency modulation. From Fig. 17 it is clear that a control strategy based on varying the frequency of a desired output  $y_d(t) = A_r \sin(2\pi f_r t)$ , with  $A_r$  fixed, can be used to generate a given output average lift force  $F_L(t)$ . Thus, a desired average lift force  $F_L^*(t)$  or a desired altitude  $x_d(t)$  can be followed. Detailed analyses and experimental results for frequency modulation is the subject of future work. However, here we show through an experiment that the proposed control scheme in Fig. 5 is suitable for implementing control strategies based on frequency modulation. In Fig. 19, the experimental results show the transition of the frequency  $f_r$  from 105 Hz to 135 Hz of the desired output signal  $y_d = A_r \sin(2\pi f_r t)$  and the measured signal  $y(t)$ , in red and blue, respectively. Here, the upper plot shows in steady-state the signals  $y_d(t)$ , with  $f_r = 105$  Hz, and  $y(t)$ . At  $Time = 5$  s, the desired frequency  $f_r$  is switched from 105 to 135 Hz, as can be seen in the middle plot of Fig. 19. It is clear that  $y(t)$  reaches steady-state in 0.12 s approximately. The bottom plot shows that  $y(t)$  accurately follows  $y_d(t)$  after the transition.

Fig. 20 shows the evolution of the adaptive parameters  $\alpha(t)$  and  $\beta(t)$ , as the reference frequency is changed. Here, it can be observed that for a constant  $f_r$  both parameters are approxi-

mately constant with small oscillations around their mean value. At  $Time = 5$  s, when  $f_r$  is varied from 105 Hz to 135 Hz both parameters adapt until they reach values that are approximately constant again. Figs. 19 and 20 demonstrate that frequency transitions are achievable using the adaptive algorithm and thus lift force control (and consequently altitude control) is feasible employing control strategies based on frequency modulation.

## V. EXPERIMENTAL EXAMPLES OF LIFT CONTROL AND HOVERING

### A. Lift Force Control Example

In this subsection, we present a hardware-in-the-loop experimental example of altitude control. Since the main idea is to demonstrate lift control using the adaptive scheme in Fig. 6, we employ a simple open-loop upper level control law. The objective is to follow a desired average lift force signal,  $F_L^*(t)$ , such that a 70-mg robotic fly would move from 0 to 0.3 m and then return to 0 m in no more than 3 s. Using the model in Subsection II-A and the experimental data in Fig. 17, through computer simulation the complying *a priori* trajectory in Fig. 21 was found. Also according to the simulation, the *a priori* trajectory in Fig. 21 is achievable by tracking the desired average lift force signal in red in Fig. 22, where  $N_L = 1000$ .

The resulting experimental average lift force is plotted in blue in Fig. 22, which using the control strategy in Fig. 6 of Section IV, results from choosing  $r(t) = -y_d(t) = -A_r \sin(2\pi \cdot 150t)$ , with  $A_r = 1.2$  for  $t \in [0, 0.347)$  s and  $A_r = 0.95$  for  $t \in [0.347, 5]$  s. The time series of the reference,  $y_d(t)$ , and output,  $y(t)$ , are shown in Fig. 23. Here, on the left the complete signals are compared, and on the right the transition from  $A_r = 1.2$  to  $A_r = 0.95$  is shown. Notice that  $y(t)$  is capable of following  $y_d(t)$  and that the transition is smooth, because  $P(z)$  is under the control of the feedforward scheme in Fig. 6. According to the simulations, the estimated resulting *a posteriori* trajectory is shown in blue in Fig. 21, which indicates that more sophisticated upper level control laws are required for achieving complex trajectories.

### B. Hovering Example

The purpose of this subsection is to demonstrate how the ideas and the methods described in this article are a key step in achieving the final goal of designing, fabricating and controlling completely autonomous flying microrobots. One way of thinking of the previous results is that through the presented static experiments, a significant amount of information can be obtained in order to design higher level control strategies for achieving hovering and for following *a priori* chosen desired vertical trajectories. In this subsection, we show the efficacy of this approach with a demonstration of controlled hovering for an insect-inspired microrobot. The experimental and theoretical details behind these results escape the scope of this paper and will be presented in a future publication. In the context of this work, the important point is to present additional evidence proving that using amplitude modulation of the actuator displacement, and consequently, of the microrobot's wing flapping

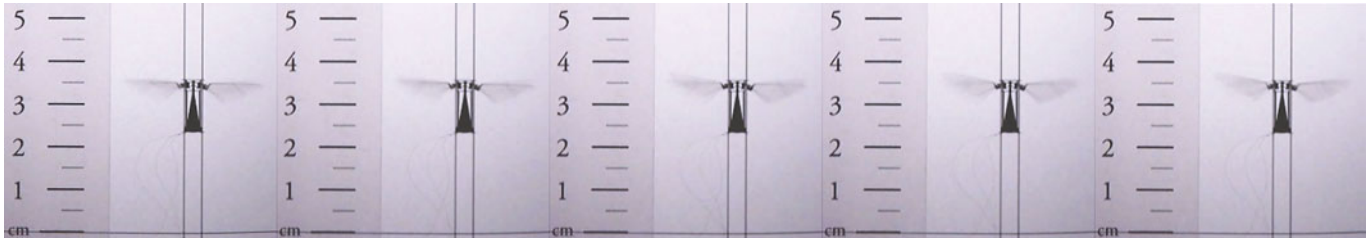


Fig. 25. Sequence of video frames showing a flapping-wing flying microrobot hovering at an altitude of 2.5 cm. The side ruler is placed as a rough reference not for exact measurement of the flying robot's altitude. The exact vertical position  $x(t)$  is measured using a laser displacement sensor. The sampling time at which the frames were taken is approximately 31.9 ms. The complete experiment is shown in the supporting movie S1 at [35].

angle, hovering is achievable by balancing the robot's weight with the generated average lift force.

For this hovering demonstration we use the 56-mg flying microrobot in Fig. 24. Here, the objective is to generate an average lift force of 56 mg in order to overcome the microrobot's weight, and therefore, force the artificial fly to hover at a desired altitude (2.5 cm in this case). A photographic sequence of a hovering experiment is shown in Fig. 25. The complete experiment can be seen in the supplemental movie S1 at [35]. In this case, the lift force cannot be measured directly and a feedback upper level control strategy as depicted in Fig. 18 is employed. The altitude  $x(t)$  of the fly is measured using a large-range CCD laser displacement sensor (LK-2001 fabricated by Keyence), where the altitude reference  $x_d(t)$  is set to 2.5 cm.

It is worth mentioning that the experimental results presented in Subsection V-A and in this subsection are a key step in the path for achieving the goal of designing, fabricating, and controlling completely autonomous *micro air vehicles* (MAVs), since these experiments demonstrate unequivocally that forces can be modulated by varying the amplitudes and frequencies of the stroke angles. Nevertheless, in order to achieve complete control of MAVs, new mechanical designs must be developed. During the last decade, experimental results on the mechanical design and fabrication of flapping propulsion systems for MAVs with the potential for producing lift forces capable of overcoming gravity have been reported [34], [36], [37]. However, the subject of mechanical design for autonomous control is still a matter of further research.

## VI. CONCLUSION AND FUTURE WORK

In this paper, we presented an investigation on the issue of enforcing desired trajectories on microrobotic insects in vertical flight and hovering. We argued using analyses and experimental data that the original problem can be converted into one of average lift force control, and finally, into one of tracking of actuator displacement motion. In order to test the concepts introduced here, we used a single-wing static flapping mechanism and a 56-mg two-wing microrobot. In the future, we will further investigate several issues that remain open, among others, the design of upper-level control strategies, the nonlinear modeling of the mapping from actuator displacement to lift force, and the experimental implementation of the control strategy on a two-wing autonomous flying microrobot.

## APPENDIX

### MATRICES OF THE STATE SPACE REPRESENTATION OF THE IDENTIFIED PLANT $\hat{P}(z)$

$$A_P = \begin{bmatrix} 0.9920 & -0.0684 & 0.0148 & 0.0346 \\ 0.0684 & 0.9602 & 0.1562 & 0.0089 \\ 0.0148 & -0.1562 & 0.8619 & -0.4068 \\ -0.0346 & 0.0089 & 0.4068 & 0.8308 \end{bmatrix}$$

$$B_P = \begin{bmatrix} -0.0327 \\ 0.0591 \\ 0.0632 \\ -0.0562 \end{bmatrix}$$

$$C_P = [-0.4644 \quad -0.8401 \quad 0.8980 \quad 0.7987]$$

$$D_P = 0.$$

## REFERENCES

- [1] R. J. Wood, "The first takeoff of a biologically inspired at-scale robotic insect," *IEEE Trans. Robot.*, vol. 24, no. 2, pp. 341–347, Apr. 2008.
- [2] J. P. Whitney and R. J. Wood, "Aeromechanics of passive rotation in flapping flight," *J. Fluid Mech.*, vol. 660, pp. 197–220, Oct. 2010.
- [3] B. M. Finio, N. O. Pérez-Arancibia, and R. J. Wood, "System identification and linear time-invariant modeling of an insect-sized flapping-wing micro air vehicle," in *Proc. IEEE/RSJ Int. Conf. Intell. Robots Syst.*, San Francisco, CA, Sep. 2011, to be published.
- [4] R. Dudley, *The Biomechanics of Insect Flight*. Princeton, NJ: Princeton Univ. Press, 2000.
- [5] F.-O. Lehmann and M. H. Dickinson, "The control of wing kinematics and flight forces in fruit flies (*drosophila* spp.)," *J. Exp. Biol.*, vol. 201, no. 3, pp. 385–401, Feb. 1998.
- [6] B. A. Francis and W. M. Wonham, "The internal model principle of control theory," *Automatica*, vol. 12, no. 5, pp. 457–465, Sep. 1976.
- [7] M. Tomizuka, T.-C. Tsao, and K.-K. Chew, "Analysis and synthesis of discrete-time repetitive controllers," *ASME J. Dyn. Syst., Meas., Control*, vol. 111, no. 3, pp. 353–358, Sep. 1989.
- [8] M. Tomizuka, "Zero phase error tracking algorithm for digital control," *ASME J. Dyn. Syst., Meas., Control*, vol. 109, no. 1, pp. 65–68, Mar. 1987.
- [9] S. Hara, Y. Yamamoto, T. Omata, and M. Nakano, "Repetitive control system: A new type servo system for periodic exogenous signals," *IEEE Trans. Autom. Control*, vol. 33, no. 7, pp. 659–668, Jul. 1998.
- [10] T. Inoue, M. Nakano, T. Kubo, S. Matsumoto, and H. Baba, "High accuracy control of a proton synchrotron magnet power supply," in *Proc. IFAC World Congr.*, Kyoto, Japan, Aug. 1981, pp. 3137–3142.
- [11] N. O. Pérez-Arancibia, T.-C. Tsao, and J. S. Gibson, "A new method for synthesizing multiple-period adaptive-repetitive controllers and its application to the control of hard disk drives," *Automatica*, vol. 46, no. 7, pp. 1186–1195, Jul. 2010.
- [12] A. Sacks, M. Bodson, and P. Khosla, "Experimental results of adaptive periodic disturbance cancellation in a high performance magnetic disk drive," *ASME J. Dyn. Syst., Meas., Control*, vol. 118, no. 3, pp. 416–424, Sep. 1996.

- [13] J. Levin, N. O. Pérez-Arancibia, P. A. Ioannou, and T.-C. Tsao, "A neural-networks-based adaptive disturbance rejection method and its application to the control of hard disk drives," *IEEE Trans. Magn.*, vol. 45, no. 5, pp. 2140–2150, May 2009.
- [14] P. S. Sreetharan and R. J. Wood, "Passive aerodynamic drag balancing in a flapping-wing robotic insect," *J. Mech. Design*, vol. 132, no. 5, pp. 051 006–1–11, May 2010.
- [15] R. J. Wood, K.-J. Cho, and K. Hoffman, "A novel multi-axis force sensor for microrobotics applications," *Smart Mater. Struct.*, vol. 18, no. 12, pp. 125 002–1–7, Dec. 2009.
- [16] R. J. Wood, E. Steltz, and R. S. Fearing, "Nonlinear performance limits for high energy density piezoelectric bending actuators," in *Proc. IEEE Int. Conf. Robot. Autom.*, Barcelona, Spain, Apr. 2005, pp. 3633–3640.
- [17] Y. M. Ho, G. Xu, and T. Kailath, "Fast identification of state-space models via exploitation of displacement structure," *IEEE Trans. Autom. Control*, vol. 39, no. 10, pp. 2004–2017, Oct. 1994.
- [18] N. O. Pérez Arancibia, S. Gibson, and T.-C. Tsao, "Adaptive control of MEMS mirrors for beam steering," in *Proc. ASME Int. Mech. Eng. Cong. Expo.*, Anaheim, CA, Nov. 2004, Paper IMECE2004–60256.
- [19] N. O. Pérez Arancibia, *Adaptive Control of Opto-Electro-Mechanical Systems for Broadband Disturbance Rejection*. Ph.D. Dissertation, University of California, Los Angeles, CA, 2007.
- [20] G. E. Dullerud and F. Paganini, *A Course in Robust Control Theory*. New York: Springer-Verlag, 2000.
- [21] T. Kailath, *Linear Systems*. Englewood Cliffs, NJ: Prentice-Hall, 1980.
- [22] C.-T. Chen, *Linear System Theory and Design*. New York, NY: Oxford Univ. Press, 1999.
- [23] K. Zhou and J. C. Doyle, *Essentials of Robust Control*. Upper Saddle River, NJ: Prentice-Hall, 1998.
- [24] S. Skogestad and I. Postlethwaite, *Multivariable Feedback Control*. Chichester, U.K.: Wiley, 1996.
- [25] A. J. Laub, M. T. Heath, C. C. Paige, and R. C. Ward, "Computation of system balancing transformations and other applications of simultaneous diagonalization algorithms," *IEEE Trans. Autom. Control*, vol. 32, no. 2, pp. 115–122, Feb. 1987.
- [26] P. Van Overschee and B. De Moor, *Subspace Identification for Linear Systems*. Boston, MA: Kluwer, 1996.
- [27] L. Ljung, *System Identification*. Upper Saddle River, NJ: Prentice-Hall, 1999.
- [28] T. Katayama, *Subspace Methods for System Identification*. London, UK: Springer-Verlag, 2005.
- [29] C. P. Ellington, "The aerodynamics of hovering insect flight. VI. Lift and power requirements," *Phil. Trans. R. Soc. Lond. B*, vol. 305, no. 1122, pp. 145–185, Feb. 1984.
- [30] T. Weis-Fogh, "Quick estimates of flight fitness in hovering animals, including novel mechanisms for lift production," *J. Exp. Biol.*, vol. 59, no. 1, pp. 169–230, Aug. 1973.
- [31] D. Chen and B. Paden, "Adaptive linearization of hybrid step motors: Stability analysis," *IEEE Trans. Autom. Control*, vol. 38, no. 6, pp. 874–887, Jun. 1993.
- [32] M. Bodson, A. Sacks, and P. Khosla, "Harmonic generation in adaptive feedforward cancellation schemes," *IEEE Trans. Autom. Control*, vol. 39, no. 9, pp. 1939–1944, Sep. 1994.
- [33] S. J. Elliott, I. M. Stothers, and P. A. Nelson, "A multiple error LMS algorithm and its application to the active control of sound and vibration," *IEEE Trans. Acoust., Speech, Signal Process.*, vol. 35, no. 10, pp. 1423–1434, Oct. 1987.
- [34] S. H. McIntosh, S. K. Agrawal, and Z. Khan, "Design of a mechanism for biaxial rotation of a wing for a hovering vehicle," *IEEE/ASME Trans. Mechatronics*, vol. 11, no. 2, pp. 145–153, Apr. 2006.
- [35] N. O. Pérez-Arancibia, J. P. Whitney, and R. J. Wood, "S1," *micro.seas.harvard.edu/TMECH2011/S1.mp4*, Jul. 2011.
- [36] M. Sitti, "Piezoelectrically actuated four-bar mechanism with two flexible links for micromechanical flying insect thorax," *IEEE/ASME Trans. Mechatronics*, vol. 8, no. 1, pp. 26–36, Mar. 2003.
- [37] R. Madangopal, Z. A. Khan, and S. K. Agrawal, "Energetics-based design of small flapping-wing micro air vehicles," *IEEE/ASME Trans. Mechatronics*, vol. 11, no. 4, pp. 433–438, Aug. 2006.



**Néstor O. Pérez-Arancibia** (S'05–M'08) received the Ph.D. degree in mechanical engineering from the Mechanical and Aerospace Engineering Department, University of California, Los Angeles (UCLA), CA, in 2007.

From October 2007 to March 2010, he was a Postdoctoral Scholar with the Laser Beam Control Laboratory and also with the Mechatronics and Controls Laboratory in the Mechanical and Aerospace Engineering Department at UCLA. Since April 2010, he has been a Postdoctoral Fellow with the Micro-

robotics Laboratory and the Wyss Institute for Biologically Inspired Engineering at Harvard University, Cambridge, MA. His current research interests include microrobotics, feedback control, adaptive filtering, adaptive optics, and mechatronics.



**John P. Whitney** received the S.B. degree in physics, and the S.M. degree in aerospace engineering, in 2004 and 2006, respectively, from the Massachusetts Institute of Technology (MIT), Cambridge, MA. He is working toward the Ph.D. degree in mechanical engineering at Harvard University, Cambridge, MA.



**Robert J. Wood** (M'01) received the Masters and Ph.D. degrees in electrical engineering and computer sciences from the Department of Electrical Engineering and Computer Sciences, University of California, Berkeley, CA, in 2001 and 2004, respectively.

He is currently an Associate Professor in the School of Engineering and Applied Sciences and the Wyss Institute for Biologically Inspired Engineering at Harvard University, Cambridge, MA. His research interests are in the areas of microrobotics and bio-

inspired robotics.